



# Engineering defect-rich Fe-doped NiO coupled Ni cluster nanotube arrays with excellent oxygen evolution activity

Yaqi Lei<sup>a,1</sup>, Tingting Xu<sup>a,1</sup>, Shenghua Ye<sup>a,1</sup>, Lirong Zheng<sup>d</sup>, Peng Liao<sup>e</sup>, Wei Xiong<sup>a</sup>, Jing Hu<sup>a</sup>, Yajie Wang<sup>a</sup>, Jingpeng Wang<sup>a</sup>, Xiangzhong Ren<sup>a</sup>, Chuanxin He<sup>a</sup>, Qianling Zhang<sup>a,\*</sup>, Jianhong Liu<sup>a,c,\*\*</sup>, Xueliang Sun<sup>b,\*</sup>

<sup>a</sup> College of Chemistry and Environmental Engineering, Graphene Composite Research Center, Shenzhen University, Shenzhen, 518060, PR China

<sup>b</sup> Department of Mechanical and Materials Engineering, University of Western Ontario, London, Ontario N6A 5B9, Canada

<sup>c</sup> Shenzhen Eigen-Equation Graphene Technology Co. Ltd., Shenzhen, 518000, PR China

<sup>d</sup> Institute of High Energy Physics Chinese Academy of Sciences, Beijing, 100049, PR China

<sup>e</sup> Department of Cell Research and Development, Farasis Energy Inc., Hayward, California, 94545, USA

## ARTICLE INFO

### Keywords:

Hollow nanotube arrays  
Fe-doped NiO  
Oxygen evolution reaction  
d-band  
Nonconcerted  
Proton-electron transfer

## ABSTRACT

Herein we present a novel multi-level structure of Fe-doped NiO coupled Ni cluster hollow nanotube arrays (Fe-NiO-Ni CHNAs) grown on carbon fiber cloth as an efficient catalyst for oxygen evolution reaction. In this multi-level structure, rocksalt-type Fe-doped NiO phase hybrids with Ni clusters coupled into the nanospheres anchored to the outside of nanotube, forming a unique 3D corn-like structure. This novel multi-level structure represents a large specific area for catalytic reaction. X-ray absorption fine structure indicates that the defect-rich Fe-doped NiO phase has abundant coordinative unsaturated sites as active sites, and Fe doping downshifts the d-band of metal sites, which is the main contribution to the improved oxygen evolution reaction catalytic activity. The OER of Fe-NiO-Ni CHNAs obeys the adsorbate evolution mechanism with the nonconcerted proton-electron transfer pathway as a rate-determining step. Thus Fe-doped NiO CHNAs exhibits excellent OER performance and outstanding durability that surpasses most of transition metal oxides.

## 1. Introduction

Water splitting is an effective strategy for reserving electrical energy in the form of hydrogen, which serves as a promising candidate for green energy applications, owing to its high energy density and gas-free greenhouse emission. [1] Furthermore, new generation fuel cells such as rechargeable metal-air batteries also employ water splitting at the anode during battery charge. [2,3] Water splitting involves a hydrogen evolution reaction (HER) at the cathode and an oxygen evolution reaction (OER) at the anode. However, OER is a four-electron coupling process that suffers from high overpotential and inefficiency because of the high kinetic barrier. Therefore, the sluggish kinetic energy of OER becomes the bottlenecks of water splitting and the charging of metal-air batteries [4,5]. Designing high-performance OER electrocatalysts thus is a key step for solving the above-noted problems.

Precious metal oxides such as IrO<sub>2</sub> and RuO<sub>2</sub> are generally considered as the best catalysts because they deliver a high catalytic activity at low overpotential. However, they are limited by their high-cost and low global reserves. Moreover, the major problem of Ru and Ir-based catalysts is that they easily dissolve and degrade at a high anodic potential. [6] Thus, developing transition metal-based electrocatalysts for OER at a low cost and with high catalytic activity and stability meets great desire. Ni-, Co-, and Fe-based oxides are promising electrocatalysts for OER and can be clarified into two main categories: spinel and perovskite oxides [7]. Spinel-type oxides such as Co<sub>3</sub>O<sub>4</sub> [8,9], NiFe<sub>2</sub>O<sub>4</sub> [10], CoFe<sub>2</sub>O<sub>4</sub> [11, 12], and ZnCo<sub>2</sub>O<sub>4</sub> [13,14] have been widely studied. Perovskite-type oxides such as LaCoO<sub>3</sub> [15], LaNiO<sub>3</sub> [16], Ce<sub>0.9</sub>Gd<sub>0.1</sub>O<sub>2.8</sub> [17], and Ba<sub>0.5</sub>Sr<sub>0.5</sub>Co<sub>0.8</sub>Fe<sub>0.2</sub>O<sub>3.8</sub> [18] have also been designed for OER and received significant improvement in terms of catalytic activity and stability in alkalines. The crucial effect of coordinative geometry and

\* Corresponding authors.

\*\* Corresponding author at: College of Chemistry and Environmental Engineering, Graphene Composite Research Center, Shenzhen University, Shenzhen, 518060, PR China.

E-mail addresses: [zhql@szu.edu.cn](mailto:zhql@szu.edu.cn) (Q. Zhang), [liujh@szu.edu.cn](mailto:liujh@szu.edu.cn) (J. Liu), [xsun9@uwo.ca](mailto:xsun9@uwo.ca) (X. Sun).

<sup>1</sup> These authors contributed equally to this work.

electronic structure of active sites on OER activity have been clarified using the combination of experiments and theoretical calculation. Octahedral sites ( $\text{MO}_6$ , where M represents metal elements) in spinel and perovskite-type oxides were identified as the actual active sites for OER. [8,19,20] Furthermore, considerable research efforts for exploring benchmarking the catalytic activities of transition-metal-based (Ni, Co, Fe, Mn, etc.) catalysts at over the past 60 years, a holistic perspective is that Fe-containing transition-metal-based electrocatalysts are considered to be the most promising OER electrocatalysts in alkaline, and Fe doping in transition-metal-based catalysts as an effective strategy to improve OER activity of Ni- and Co-based catalysts. The crucial role of Fe was firstly proposed by Edison in 1902, and then unique effect of Fe decreases OER overpotential and changes the redox peak of Ni and Co also has been confirmed in succession. Therefore, illumination of the role of Fe in Fe-containing catalysts is important to guide the catalyst design [21–24]. Yagi et al. proposed that  $[\text{Fe}^{4+}\text{O}^6]$  was created during the OER process, and this special unites demonstrated appropriate occupation in  $e_g$  orbital; thus, Fe sites were actual active sites. [25] But other researchers proposed opposite perspectives of  $\text{Fe}^{3+}$ , such as its ability to stabilize metallic ions in high oxidation states (e.g.,  $\text{Ni}^{4+}$ ) that are active sites and thereby improving OER activity. [26,27] Many researches mainly focus on Fe doping in (oxy)hydroxides, and debate whether Fe site is actually catalytic site, while few studies concern the effect of Fe doping on modifying d-band structure which is crucial for electrocatalysis. Although the exact mechanism of Fe species' contribution to OER activity remains debatable, the importance of Fe for exploring metal oxides as effective OER catalysts is undoubted.

The spinel and perovskite oxides have been widely developed as OER catalysts. However, Rocksalt-type ( $\text{NaCl}$ -type) oxides are rarely considered as OER catalysts. These oxides are constructed by edge-shared  $\text{MO}_6$  octahedrons to form a cubic crystal system. [28] General transition metal rocksalt-type oxides include  $\text{NiO}$ ,  $\text{CoO}$ , and  $\text{FeO}$ .  $\text{NiO}$  – a stable, extensive and low-cost compound – may be an appropriate candidate for OER catalysts [29].

Inspired by the above information, we synthesized a novel structure of Fe-doped  $\text{NiO}$  coupled Ni cluster hollow nanotube arrays ( $\text{Fe-NiO-Ni}$  CHNAs). The arrays were grown on carbon fiber cloth (CFC) by in-situ anodic oxidation of metallic Ni nanorod arrays. The in-situ anodic oxidation created low crystallinity and structural defects in  $\text{Fe-NiO-Ni}$  CHNAs, while Fe-doping altered the electronic structure of  $\text{NiO}$  by lowering the d-band and endowing  $\text{Fe-NiO-Ni}$  CHNAs with excellent stability and OER activity compared with  $\text{NiO-Ni}$  CHNA counterpart. This indicated that Fe-doping is crucial for improving the OER activity of  $\text{NiO}$ . Moreover, the structural defects and Ni clusters also contributed to the improvement of OER activity.

## 2. Experimental section

### 2.1. Materials

All the chemical reagents used throughout the work were of analytical grade and used directly without further purification.

### 2.2. Catalyst preparation

The catalysts were prepared by galvanostatic electrolysis in a two-electrode cell. The counter electrode was a graphite electrode (1.8  $\text{cm}^2$ , spectral grade), and the working electrode was a carbon fiber cloth (CFC) (2  $\text{cm} \times 0.5 \text{ cm}$ ). The fabrication procedures of catalysts were as follows:

- 1)  $\text{ZnO}$  NRAs were electrodeposited on a CFC in a 10 mL 0.02 M  $\text{Zn}(\text{NO}_3)_2 + 0.1 \text{ M NH}_4\text{NO}_3$  solution at  $-0.8 \text{ mA cm}^{-2}$  for 60 min.
- 2)  $\text{ZnO@Ni}$  NRAs were fabricated by electrodeposition of Ni on  $\text{ZnO}$  nanorods in a 0.1 M  $\text{NiSO}_4 + 0.05 \text{ M H}_3\text{BO}_3 + 0.05 \text{ M NH}_4\text{AC}$  solution at  $-0.5 \text{ mA cm}^{-2}$  for 30 min.
- 3)  $\text{Fe-NiO-Ni}$  CHNAs were synthesized by in situ anodic oxidation of

$\text{ZnO@Ni}$  NRAs in a 0.01 M  $(\text{NH}_4)_2\text{Fe}(\text{SO}_4)_2$  solution at  $0.5 \text{ mA cm}^{-2}$  for 30 min, then dissolved the  $\text{ZnO}$  template by immersing the sample into a 1 M  $\text{KOH}$  solution for 3 h.

4)  $\text{NiO-Ni}$  CHNAs were synthesized as  $\text{Fe-NiO-Ni}$  CHNAs, except for the  $(\text{NH}_4)_2\text{SO}_4$  solution, which was used as electrolyte.

5) Preparation of  $\text{IrO}_2/\text{NF}$ : 5 mg  $\text{IrO}_2$  powders was dispersed into 1 mL solvent which is composed of water and ethanol ( $v/w/v = 1/4$ ) to form ink, 45  $\mu\text{L}$  5 wt% Nafion solution was added into above ink during supersonic. 105  $\mu\text{L}$  of above suspensions was pipetted onto a piece of nickel foam (NF), after evaporation in air,  $\text{IrO}_2/\text{NF}$  was prepared.

### 2.3. Catalyst characterization

Field emission scanning electron microscope (FE-SEM, JSM-6330F) and transmission electron microscope (TEM, JEM-2010 h and Tecnai F30 S-TWIN) were used to characterize the morphology of catalysts. X-Ray diffraction (Rigaku D/max 2500/PC) and Raman spectroscopy (Renishaw, inVia) were employed to confirm the chemical structure. Chemical-state analysis was performed by X-Ray photoelectron spectroscopy (XPS) (ESCAKAB 250). All peaks were corrected by C 1s line at 284.8 eV as standard. Inductively coupled plasma-atomic emission spectrometry (ICP-AES) (TJA IRIS (HR)) spectrometer was used to measure the metal loading and ratio. X-ray absorption fine structure measurements: the X-ray absorption fine structure (XAFS) spectra were recorded at the 1W1B station of the Beijing Synchrotron Radiation Facility (BSRF).

### 2.4. Electrochemical measurements

Electrochemical measurements were performed by CHI 660E electrochemical analyzer (CH Instruments, Inc., Shanghai), a graphite rod and a mercuric oxide electrode (MOE) was used as counter electrode and reference electrode respectively. The potential was calibrated with respect to the reversible hydrogen electrode (RHE) by the following equation:  $E(\text{RHE}) = E(\text{vs. HgO/Hg}) + 0.098 \text{ V} + 0.059 \text{ pH}$ .

### 2.5. DFT calculation

All the calculations in this work were performed by the Vienna Ab-initio Simulation Package (VASP) [30–31] based on density functional theory (DFT). The Perdew-Burke-Ernzerhof (PBE) functional forms of the generalized gradient approximation (GGA) were used to describe the electron-electron exchange-correlation interactions. [32,33] The Van der Waals interaction was corrected by D2 method in all the calculations [34]. A plane-wave cutoff energy was set to be 520 eV with the k-point meshes of  $9 \times 9 \times 9$  and  $5 \times 5 \times 1$  were used for  $\text{NiO}$  bulk and the Fe doped- $\text{NiO}$  (110), respectively. The Fe doped- $\text{NiO}$  (110) and the intermediates adsorption were all modeled by a  $3 \times 3 \times 1$  supercells. The vacuum layer of 20 Å was used to eliminate the interaction between adjacent layers. The convergence accuracy of the total energy and the force during the structural relaxation was  $10^{-5} \text{ eV}$  and  $-0.01 \text{ eV}/\text{Å}$ , respectively. The Spin-polarized were taken into account throughout the calculations.

The adsorption free energies were obtained by including the zero point energy (ZPE) and the entropy (S) corrections in equation

$$\Delta G = \Delta E + \Delta \text{ZPE} - T\Delta S + \Delta G_U$$

Where  $\Delta E$  was reaction heats of a certain reaction step,  $\Delta G_U = -eU$  with  $U$  being the electrode potential. The  $\Delta \text{ZPE}$  could be obtained from the calculation of vibrational frequencies for the adsorbed species, and the  $T$  was temperature. The free energy of  $\text{O}_2$  was obtained from the reaction  $4\text{OH}^- = 2\text{H}_2\text{O} + \text{O}_2$  for which the free energy change was 4.92 eV.

### 3. Results and discussion

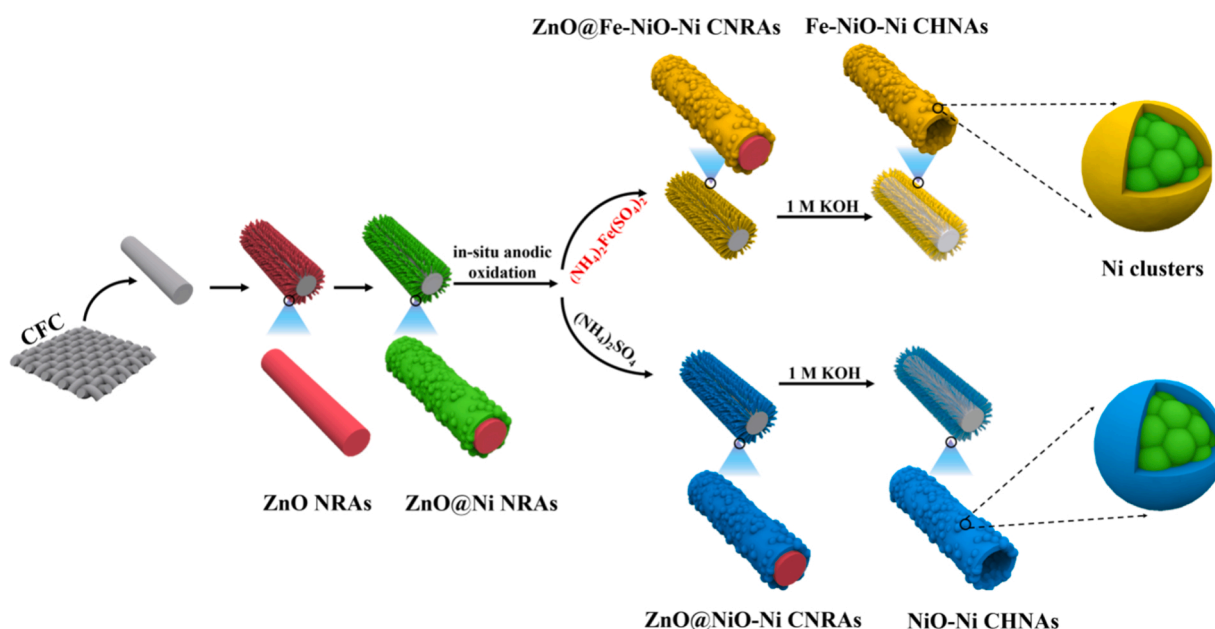
#### 3.1. Morphology and structure

The synthetic processes of Fe-NiO-Ni CHNAs and NiO-Ni CHNAs are shown in **Scheme 1**. First, ZnO nanorods arrays (ZnO NRAs) were grown on CFC by electrodeposition. Then, ZnO@Ni NRAs were fabricated by electroreduction of  $\text{Ni}^{2+}$  on the surfaces of ZnO nanorods. Subsequently, ZnO@Ni NRAs were oxidized by in-situ anodic oxidation in  $(\text{NH}_4)_2\text{Fe}(\text{SO}_4)_2$  solution. Finally, ZnO templates were removed by NaOH solution, and Fe-NiO-Ni CHNAs were fabricated. The counterpart of Fe-NiO-Ni CHNAs without Fe-doping was synthesized as NiO-Ni CHNAs using  $(\text{NH}_4)_2\text{SO}_4$  solution via the in-situ anodic oxidation process.

Scanning electron microscopy (SEM) images of CFC and ZnO NRAs are shown in **Figures S1** and **S2**, respectively. As shown in **Figures S2** and **S3**, the ZnO nanorods were uniformly grown on a three-dimensional (3D) CFC substrate. Following electrodeposition of metallic Ni on ZnO nanorods, the ZnO nanorods were coated with metallic Ni and some nanospheres were attached to the surface of ZnO@Ni nanorods to form a corn-like structure. This can clearly be seen in the SEM and transmission electron microscope (TEM) images shown in **Figures S4** and **S5**, respectively. The X-ray powder diffraction (XRD) pattern also showed that metallic Ni was formed after electrodeposition (**Figure S6**). Following in-situ anodic oxidation, ZnO@Fe-NiO-Ni CNRAs was formed. Its morphology was the same as that of ZnO@Ni NRAs with no obvious changes as shown in **Figure S7**. After removing the ZnO templates, Fe-NiO-Ni CHNAs were synthesized. The SEM image of Fe-NiO-Ni CHNAs in **Fig. 1a** shows that the structure of nanotube arrays was formed, the hollow structure can clearly be observed and the nanospheres were attached to the external wall of Fe-NiO-Ni CHNAs, as shown in the magnified SEM image (**Fig. 1b**). The TEM image of Fe-NiO-Ni CHNAs (**Fig. 1c**) suggests that the hollow nanotube structure was formed by removing the ZnO templates, and the nanospheres anchored on the external wall of nanotube can also clearly be seen, which is consistent with SEM images. The high-resolution transmission electron microscopy (HRTEM) image of Fe-NiO-Ni CHNAs is shown in **Fig. 1d**. No continual lattice was observed. Therefore, we concluded that Fe-NiO-Ni CHNAs exhibited low crystallinity. Moreover, the morphology of NiO-Ni CHNAs is shown in **Fig. 1e** and **g**. As shown in SEM (**Fig. 1e** and **f**) and TEM (**Fig. 1g**) images, NiO-Ni CHNAs included similar hollow nanotubes with

nanospheres anchored on the external wall to form a corn-like morphology, and the crystallinity of NiO-Ni CHNAs was also extremely low (**Fig. 1h**).

To further characterize the components of Fe-NiO-Ni CHNAs and NiO-Ni CHNAs, inductively coupled plasma atomic emission spectroscopy (ICP-AES), XRD pattern, X-ray photoelectron spectroscopy (XPS) and Raman spectroscopy were employed. ICP-AES result showed the molar ratio of Ni:Fe in Fe-NiO-Ni CHNAs as 4:1. Moreover, there isn't any product could be found if the in-situ oxidation was performed on the bare CFC (**Figure S9**), indicating that Fe was introduced during the transformation from metallic Ni to NiO. XRD patterns of Fe-NiO-Ni CHNAs and NiO-Ni CHNAs depicted in **Fig. 2a** showed that no diffraction peak was found (except for CFC signals). This suggested low crystallinity of Fe-NiO-Ni CHNAs and NiO-Ni CHNAs. The chemical states of samples were characterized via XPS (C1 s and O1 s spectra are shown in **Figures S10** and **S11**). The Ni 2p spectra are shown in **Fig. 2b**. Here, the peaks at  $\sim 855$  eV and  $\sim 873$  eV were attributed to  $\text{Ni}^{2+}$ . Surprisingly, the peak at  $\sim 852$  eV was attributed to metallic Ni, indicating that both  $\text{Ni}^{2+}$  and  $\text{Ni}^0$  existed in Fe-NiO-Ni CHNAs and NiO-Ni CHNAs. The negative shift in the binding energy of Ni 2p in Fe-NiO-Ni CHNAs indicated the existence of strong electronic interaction between Ni and Fe, which altered the electronic structure of Ni. The lower chemical binding energy of Ni 2p indicated the weaker oxophilicity of active nickel sites, which have been proven beneficial for OER. [35] The Fe 2p spectra of Fe-NiO-Ni CHNAs is shown in **Fig. 2c**, indicating that the valence of Fe is +3. Raman spectra of Fe-NiO-Ni CHNAs and NiO-Ni CHNAs are shown in **Fig. 2d**. In NiO-Ni CHNAs, Raman peaks of  $400\text{--}580\text{ cm}^{-1}$  were attributed to 1TO and 1LO of NiO, respectively, [36] [37], and the spectral features are obviously different from those of Ni(OH)<sub>2</sub> and NiOOH with a pair of bands at  $449, 530\text{ cm}^{-1}$  and  $474, 554\text{ cm}^{-1}$  [38], thus we can justify that the primary component of NiO-Ni CHNAs should be NiO rather than (oxy) hydroxides (little of metal (oxy)hydroxide may be formed on the surface during the catalysis in the electrolyte, but we haven't detected at least). To further support this speculation, NiO-Ni CHNAs was annealed at  $300^\circ\text{C}$  in air to undergo crystallization as a reference. Concurrently, metallic Ni was oxidized to NiO and eventually formed a crystalline counterpart (denoted as c-NiO HNAs) (**Figure S12**). The XRD pattern of c-NiO HNAs clearly exhibited diffraction peaks of rocksalt-type NiO (**Figure S13**). The Raman spectrum of c-NiO HNAs was similar to that of NiO-Ni CHNAs (**Figure S14**),



**Scheme 1.** Synthesis of Fe-NiO-Ni CHNAs and NiO-Ni CHNAs.

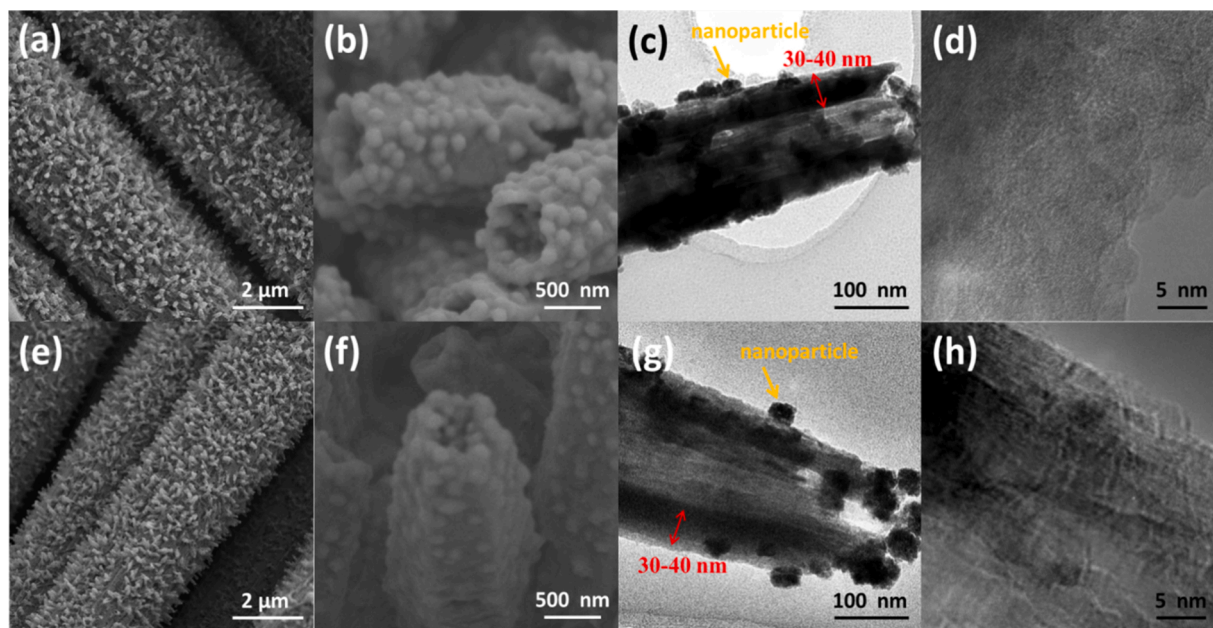


Fig. 1. (a–b and e–f) SEM images of Fe-NiO-Ni CHNAs and NiO-Ni CHNAs at different magnifications, respectively; (c–d and g–h) TEM and HRTEM images of Fe-NiO-Ni CHNAs and NiO-Ni CHNAs, respectively.

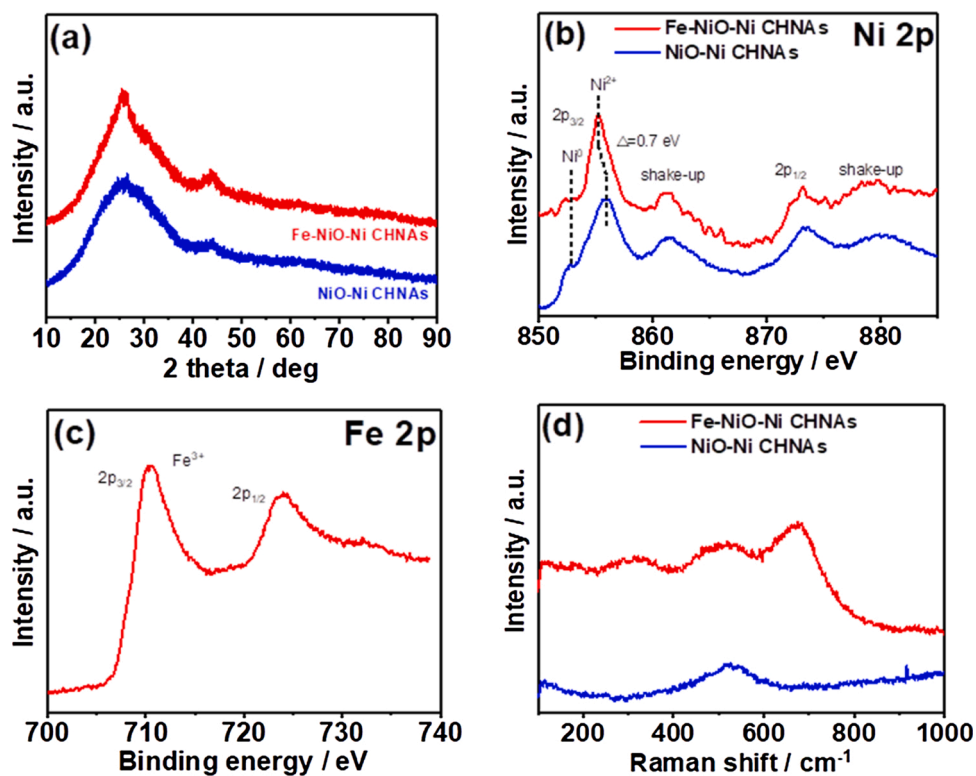


Fig. 2. (a) XRD patterns and (b) Ni 2p spectra of Fe-NiO-Ni CHNAs and NiO-Ni CHNAs; (c) Fe 2p spectra of Fe-NiO-Ni CHNAs; (d) Raman spectra of Fe-NiO-Ni CHNAs and NiO-Ni CHNAs.

further indicating that amorphous NiO existed in NiO-Ni CHNAs. For Fe-NiO-Ni CHNAs, Raman peaks of NiO still existed and were accompanied by two new peaks at 320 and 682  $\text{cm}^{-1}$ . These peaks were attributed to the vibration modes of Fe-O [39] and suggested the formation of a Fe-doped NiO structure. Moreover, electron paramagnetic resonance (EPR) results demonstrated a strong signal for Fe-NiO-Ni CHNAs and NiO-Ni CHNAs at  $g = 2.003$  (Figure S15), thereby

suggesting the existence of O vacancies. [40] The signal intensity of Fe-NiO-Ni CHNAs was much stronger than that of NiO-Ni CHNAs, and photoluminescence (PL) spectra (Figure S16) exhibited an emission peak near 400 nm, corresponding to the recombination of holes with a two-electron-trapped O vacancy, while the higher peak intensity of Fe-NiO-Ni CHNAs determined the presence of additional O vacancies, [41] indicating that Fe doping increased the concentration of O

vacancies.

To further characterize the chemical and electronic structure, X-ray absorption fine structure (XAFS) spectra were collected at the 1W1B station of the Beijing Synchrotron Radiation Facility. The X-ray absorption near edge structure (XANES) of the Ni K-edge of Fe-NiO-Ni CHNAs, NiO-Ni CHNAs, c-NiO HNAs, and Ni foil are depicted in Fig. 3a. First, the shape of the post-edge in Fe-NiO-Ni CHNAs and NiO-Ni CHNAs were similar to that of c-NiO HNAs which has been proven to be composed of crystalline NiO, except for the oscillation of Fe-NiO-Ni CHNAs and NiO-Ni CHNAs having been obviously attenuated, this represents the components of NiO phases in Fe-NiO-Ni CHNAs and NiO-Ni CHNAs. The attenuated oscillation infers a lack of long-range order [42] and agrees with the low crystalline features of Fe-NiO-Ni CHNAs and NiO-Ni CHNAs. Furthermore, the pre-edge is also a characterization of the chemical structure. The pre-edge at  $\sim 8335$  eV (noted by the red arrows in Fig. 3a) was a feature of metallic Ni. However, this characteristic pre-edge was absent in c-NiO HNAs (the pre-edge noted by the

green arrow in Fig. 3a originated from the transition of  $1s \rightarrow 3d$  in  $MO_6$  octahedrons), indicating that metallic Ni had been thoroughly oxidized after annealing in the atmosphere and transformed to crystalline NiO, as shown in the XANES of Fe-NiO-Ni CHNAs and NiO-Ni CHNAs, the pre-edge relative to metallic Ni also existed, indicating that  $Ni^0$  presented in both Fe-NiO-Ni CHNAs and NiO-Ni CHNAs, which is consistent with the XPS results.

Fourier transformed extended x-ray absorption fine structure (FT-EXAFS) is a powerful method for characterizing coordinative geometry, as shown in Fig. 3b. Two coordinative shells for c-Ni HNAs exist. The first coordinative shell can be assigned to Ni-O coordination and the second coordinative shell is attributed to the closest Ni-Ni distance between two edge-sharing octahedral sites (denoted as Ni-Ni<sub>oxide</sub>). For Ni foil, the coordinative shell can be assigned to the Ni-Ni distance (denoted as Ni-Ni<sub>metal</sub>). For Fe-NiO-Ni CHNAs and NiO-Ni CHNAs, Ni-O, Ni-Ni<sub>oxide</sub> and Ni-Ni<sub>metal</sub> were found, respectively, verifying the existence of metallic Ni in both Fe-NiO-Ni CHNAs and NiO-Ni CHNAs, which is

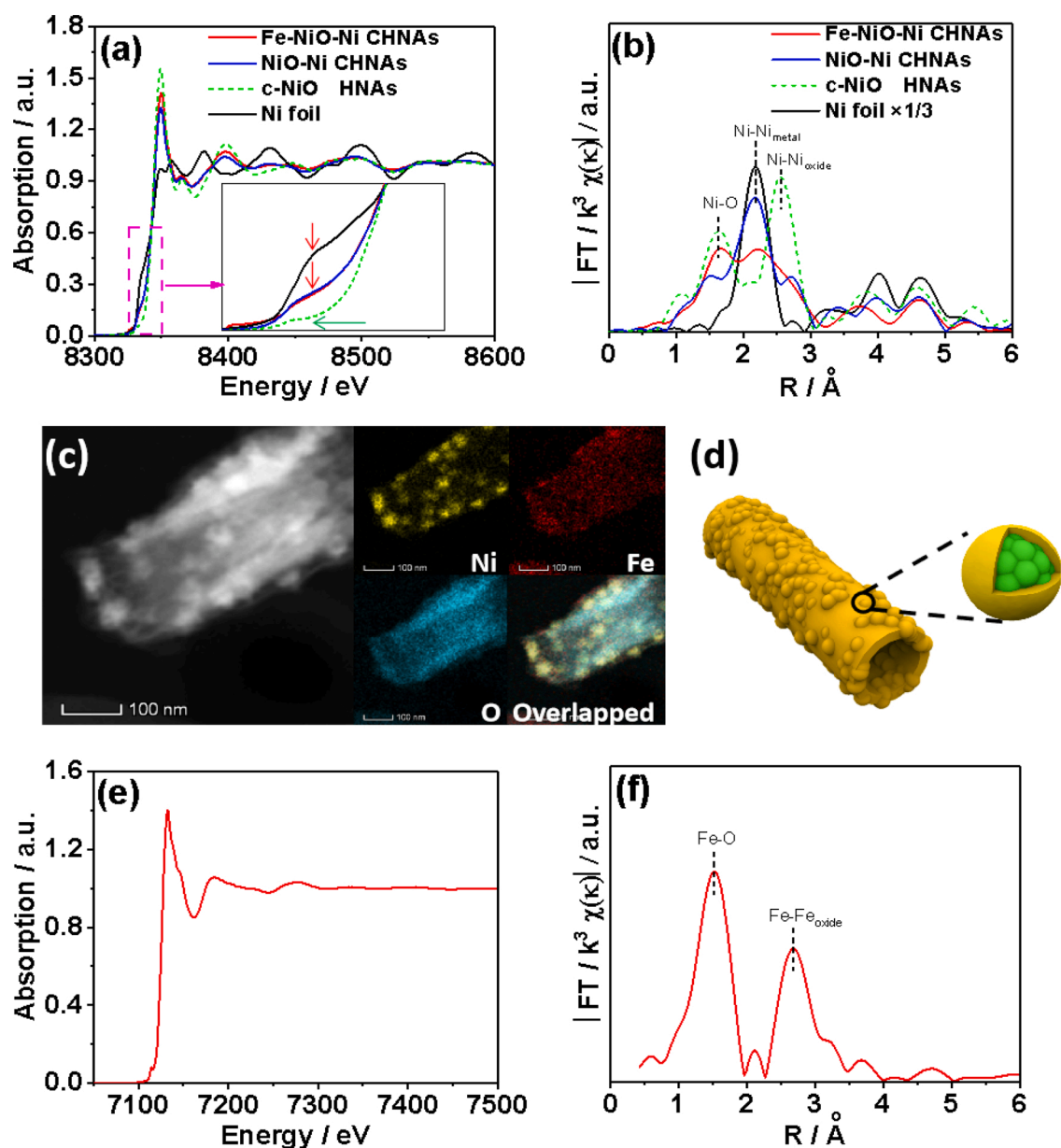
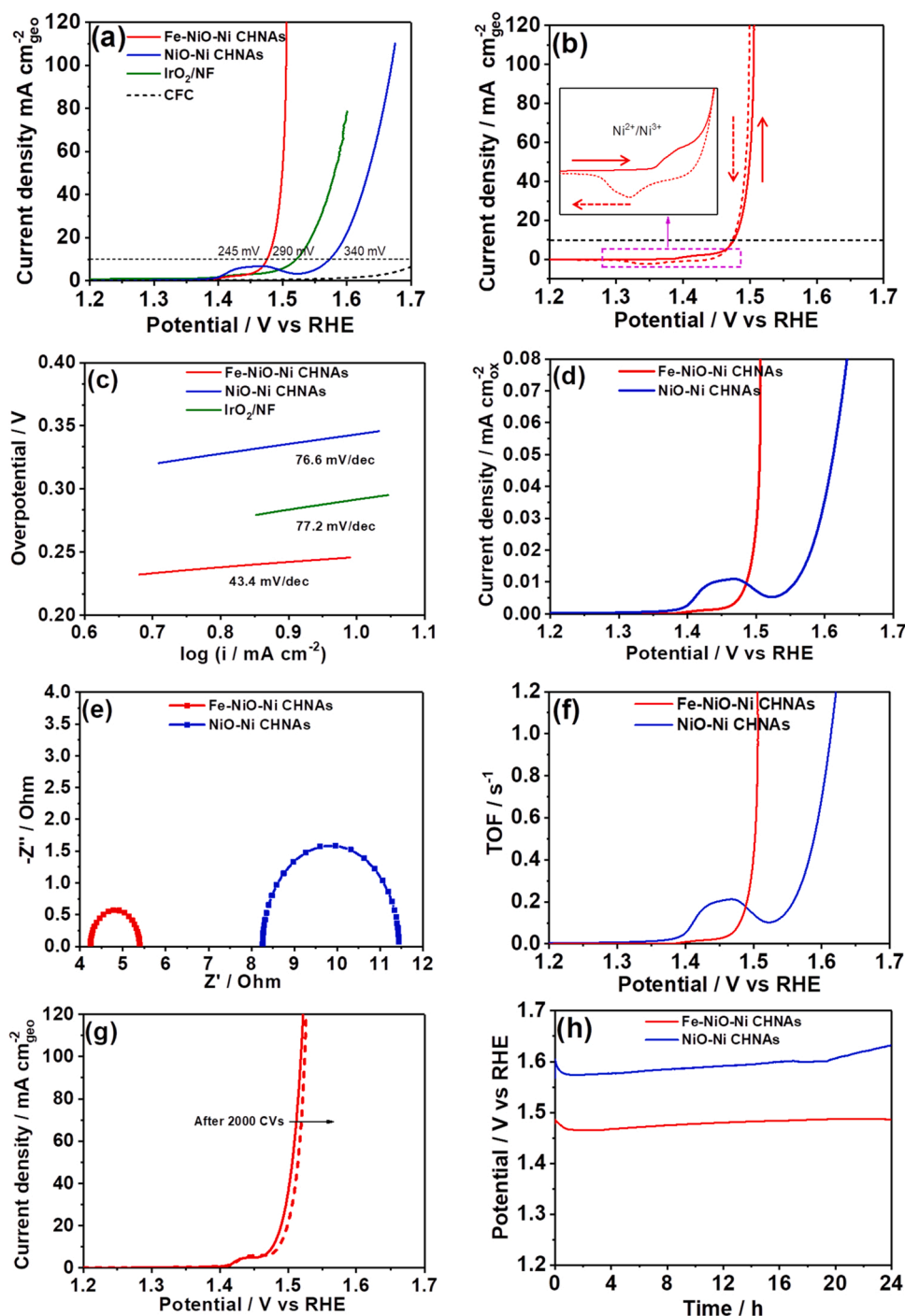


Fig. 3. (a) XANES and (b) FT-EXAFS (without phase correction) of the Ni K-edge of Fe-NiO-Ni CHNAs, NiO-Ni CHNAs, c-NiO-Ni HNAs, and Ni foil; (c) HAADF-STEM image and elemental mapping of Fe-NiO-Ni CHNAs; (d) scheme of the structure of Fe-NiO-Ni CHNAs; (e) XANES and (f) FT-EXAFS (without phase correction) of the Fe K-edge of Fe-NiO-Ni CHNAs.

consistent with XPS and XANES analyses. The fitting curves and parameters of EXAFS are shown in **Figure S18** and **Table S1**, respectively. The coordinative numbers (CN) of Ni-O and Ni-Ni<sub>ox</sub> in Fe-NiO-Ni CHNAs and NiO-Ni CHNAs were lower than that in c-NiO HNAs, indicating that the O and Ni vacancies generated by low crystallinity resulted in a high disorder that can easily form structural defects. Moreover, the CN of Ni-Ni<sub>metal</sub> in Fe-NiO-Ni CHNAs and NiO-Ni CHNAs was much lower than that in Ni foil, suggesting that metallic Ni was present in the form of Ni cluster. The high-angle annular dark field scanning transmission electron microscopy (HAADF-STEM) and corresponding elemental mapping of Fe-NiO-Ni CHNAs are shown in **Fig. 3c**. We see that Ni, Fe and O are distributed uniformly throughout the wall of nanotubes, but concentration of Ni in the nanoparticles anchored on the wall of nanotube is

relatively higher, indicating that additional Ni existed in the nanospheres (see **Fig. 3d**). The elemental mapping of NiO-Ni CHNAs (**Figure S18**) suggested a similar result. Combining the results of elemental mapping and XAFS, we speculated that Ni clusters were dispersed within the nanospheres anchored on the wall of nanotubes. The XANES and FT-EXAFS of the Fe K-edge for Fe-NiO-Ni CHNAs are shown in **Figs. 3e** and **f**. The fitting curves and parameters of FT-EXAFS are shown in **Figure S21** and **Table S2**, respectively. The CN of Fe-O and Ni/Fe-Fe were lower than 6 and 12 that represent normal CN in rocksalt structure, which verified that Fe sites were also coordinatively unsaturated. In summary, Fe-NiO-Ni CHNAs were shown to comprise a low crystalline level and a defect-rich Fe-doped NiO phase with metallic Ni clusters wrapped in the nanospheres anchored on the wall of nanotubes,



**Fig. 4.** (a) LSV curves of Fe-NiO-Ni CHNAs, NiO-Ni CHNAs, IrO<sub>2</sub>/NF, and CFC in 1 M KOH at a scan rate of 5 mV s<sup>-1</sup> after iR correction; (b) LSV curves of Fe-NiO-Ni CHNAs swept from low to high potential and high to low potential, respectively; (c) Tafel plots of Fe-NiO-Ni CHNAs, NiO-Ni CHNAs, and IrO<sub>2</sub>/NF; (d) LSV curves of Fe-NiO-Ni CHNAs and NiO-Ni CHNAs with current density normalized to the ECSA of oxides; (e) EIS plots at 1.574 V and (f) TOF curves of Fe-NiO-Ni CHNAs and NiO-Ni CHNAs; (g) LSV curves of Fe-NiO-Ni CHNAs before and after 2000 CVs; (h) E-t curves of Fe-NiO-Ni CHNAs and NiO-Ni CHNAs at current density of 10 mA cm<sup>-2</sup>.

as shown in Fig. 3d.

### 3.2. Electrochemical performances

#### 3.2.1. OER activity

The OER electrocatalytic activity of Fe-NiO-Ni CHNAs was studied by linear sweep voltammetry (LSV) in a 1.0 M KOH solution at 5 mV/s after iR-correction. NiO-Ni CHNAs and commercial IrO<sub>2</sub> coated on Ni foam (denoted as IrO<sub>2</sub>/NF) were used as reference. First, LSV curves for Fe-NiO-Ni CHNAs with different in-situ anodic oxidation times were performed. The optimized oxidation time was 30 min (Figure S22). This sample was selected as a represent for further study. The LSV curves of Fe-NiO-Ni CHNAs, NiO-Ni CHNAs, IrO<sub>2</sub>/NF, and CFC are shown in Fig. 4a. The CFC as substrate was inert to OER. Fe-NiO-Ni CHNAs displayed a much earlier onset potential than NiO-Ni CHNAs and exhibited the highest catalytic activity at a low overpotential of ~245 mV (1.475 V vs RHE) at 10 mA cm<sup>-2</sup>. Contrastingly, NiO-Ni CHNAs required an overpotential of ~340 mV (1.570 V vs RHE), indicating that Fe-doping greatly improved the catalytic activity of NiO. Moreover, the catalytic activity of Fe-NiO-Ni CHNAs even surpassed that of IrO<sub>2</sub>/NF, which requires an overpotential of ~290 mV (1.516 V vs RHE) and state-of-the-art catalysts (Table S3). It is worth noting that an anodic peak at ~1.43 V for Fe-NiO-Ni CHNAs and ~1.47 V for NiO-Ni CHNAs can be assigned to the Ni<sup>2+</sup>/Ni<sup>3+</sup> transition. [43],<sup>44</sup> This pseudocapacitive behavior may have affected the value of η<sub>10mV</sub>. To avoid this interference, the LSV curves were performed inversely. [45] [46], As shown in Fig. 4b, the value of η<sub>10mV</sub> in the inverted curve was 244 mV (1.474 V vs RHE), which was almost identical to the value of a normal LSV curve and was not obviously affected by the redox peak of Ni<sup>2+</sup>/Ni<sup>3+</sup>. The η<sub>10mV</sub> of NiO-Ni CHNAs with 361 mV (1.591 V vs RHE as shown in Figure S23) was slightly larger than the value in a normal LSV curve as shown in Fig. 4a, because the large pseudocapacitive peak of NiO-Ni CHNAs interfered with the value of η<sub>10mV</sub>. Tafel plots are shown in Fig. 4c. The Tafel slope of Fe-NiO-Ni CHNAs was only ~43.4 mV/dec, which is much lower than those of NiO-Ni CHNAs (76.6 mV/dec) and IrO<sub>2</sub>/NF (77.2 mV/dec), suggesting the rapid reactive kinetics of Fe-NiO-Ni CHNAs. Furthermore, the current density normalized by the geometric surface area of the electrode does not considered surface morphology and loading, thus cannot become a representative of real catalytic activity. [14] To further reveal the activities of Fe-NiO-Ni CHNAs and NiO-Ni CHNAs, current densities were normalized to their electrochemical specific active area (ECSA), as determined by an electrical double-layer capacitor (C<sub>dl</sub>) (Figure S24). The ECSA of Fe-NiO-Ni CHNAs and NiO-Ni CHNAs were calculated as 968.8 and 618.8 cm<sup>2</sup><sub>ox</sub>, respectively. Fe-NiO-Ni CHNAs still exhibited the highest catalytic current density after normalizing the LSV curves to the ECSA (Fig. 4d). These data clearly confirmed that the apparent catalytic activity improvement of Fe-NiO-Ni CHNAs should not merely attributed to the enlargement of surface area, intrinsic activity of active sites is crucial. Furthermore, the mass activity of Fe-NiO-Ni CHNAs also superior to that of NiO-Ni CHNAs (Figure S25).

The electrochemical impedance spectroscopy (EIS) results of Fe-NiO-Ni CHNAs and NiO-Ni CHNAs are shown in Fig. 4e (the fitting model is shown in Figure S26). In Fig. 4e, the semicircle is related to the charge-transfer resistance (R<sub>CT</sub>) at the solid and liquid interface. The lower R<sub>CT</sub> value of Fe-NiO-Ni CHNAs implies that a rapid electron transfer. Moreover, the turnover frequencies (TOFs) were used to further illustrate the instinct improvement. The number of active sites was measured by the oxidation peak current at ~1.2–1.5 V (Figure S27). [47] The TOF of Fe-NiO-Ni CHNAs (Fig. 4f) was significantly higher than that of NiO-Ni CHNAs, suggesting the enhanced intrinsic catalytic activity of Fe-NiO-Ni CHNAs. Consequently, all the above results strongly confirmed the outstanding catalytic activity of Fe-NiO-Ni CHNAs.

#### 3.2.2. OER stability

A long-term test was performed the durabilities of as-prepared

catalysts. As depicted in Fig. 4g, the activity of Fe-NiO-Ni CHNAs remained stable after 2000 cycles. Contrastingly, the activity of NiO-Ni CHNAs exhibited slight attenuation (Figure S28). The galvanostatic test at 10 mA cm<sup>-2</sup> (Fig. 4h) also indicated that overpotential of Fe-NiO-Ni CHNAs remained lower than that of NiO-Ni CHNAs during 24 h electrolysis without obvious attenuation. Moreover, the SEM image and XRD pattern (Figure S29) illustrated that Fe-NiO-Ni CHNAs maintained low crystallinity alongside the nanotube array. XPS (Figure S30), XAFS (Figure S31–32, Table S3–4) and Raman spectroscopy (Figure S33) suggested that there was no chemical structure variation in Fe-NiO-Ni CHNAs after the long-term durability test, indicating that the reconstruction during catalysis was limited. Consequently, Fe-NiO-Ni CHNAs exhibited high stability during the long-term OER catalytic process.

### 3.3. The study of structure-property relationship and mechanism

The origin of improved OER catalytic activity of Fe-NiO-Ni CHNAs was discussed as follows.

#### 3.3.1. Effects of Ni clusters and structural defects

To destroy the Ni cluster and vacancies, Fe-NiO-Ni CHNAs underwent calcination at 300 °C in atmosphere (denoted as c-Fe-NiO HNAs; the corresponding characterizations are shown in Figures S34–37). As expected, c-Fe-NiO HNAs exhibited inferior OER activity than Fe-NiO-Ni CHNAs (Figure S38), indicating that Ni clusters and structural defects contributed to catalytic activity. Hybrid metallic Ni and oxides improved electronic conductivity, which is beneficial to electrocatalysis. Furthermore, low crystallinity presented a defect-rich structure with metallic and oxygen vacancies, which could optimize the Gibbs free energy and adsorption energy of reactive intermediates, thereby improving the catalytic activity of OER. [41,48] Although c-Fe-NiO HNAs presented inferior OER activity, its catalytic current density still surpassed that of NiO-Ni CHNAs. Therefore, the effect of Fe doping should be the primary contribution to OER activity.

#### 3.3.2. Effect of Fe doping

The effect of Fe doping was emphatically studied. The L-edge of Ni detected by soft X-ray absorption fine structure (sXAFS) spectra (Fig. 5a) demonstrated that the Ni L<sub>3</sub> and L<sub>2</sub> edges – which originated from the electronic transition from Ni 2p<sub>3/2</sub> and 2p<sub>1/2</sub> orbitals to Ni 3d-O 2p hybrid orbitals, respectively, could be assigned. [49] The negative shift of Ni L<sub>3</sub> and L<sub>2</sub> edges in Fe-NiO-Ni CHNAs suggested that the energy of Ni 3d-O 2p hybrid orbitals had been downshifted by Fe doping. Considering the multiple effects caused by the overlap of the 2p core state and final 3d valence states, the single electron excitation approximation was no longer valid in the L-edge [49] Therefore, the K-edge of O was used to accurately analyze the valence band structure. As shown in Fig. 5b, the pre-edge at ~531 eV corresponded to the electronic transition from O 1s to Ni/Fe 3d-O 2p hybrid orbitals. [49] Here, the structure of M 3d-O 2p hybrid orbitals was clarified, where NiO belonged to rocksalt-type oxides constructed by edge-shared MO<sub>6</sub> octahedrons to form a cubic crystal system. For the MO<sub>6</sub> octahedron, the d<sub>x<sup>2</sup>-y<sup>2</sup></sub> and d<sub>z<sup>2</sup></sub> orbitals of central metallic ions showed a strong spatial overlap with O 2p orbitals, forming σ-bonding and σ\*-antibonding states (referred to as e<sub>g</sub> states) (Figure S39a and b). The d<sub>xy</sub>, d<sub>yz</sub>, and d<sub>xz</sub> orbitals exhibited weaker spatial overlap with O 2p orbitals and formed π-bonding and π\*-antibonding states (referred to as t<sub>2g</sub> states), as shown in Figure S39c and d. Some O 2p states do not hybridize with metal d-states and thus form nominally nonbonding (σ<sub>0</sub>) states, these non-bonding states alone do not contribute to the diversity of physical properties in oxides. The structure of molecular orbitals is depicted in Fig. 5c. The molecular orbitals described above became electronic bands in oxide crystals due to the translational symmetry of the unit cell. The band that originated from σ\*-antibonding and π\*-antibonding states

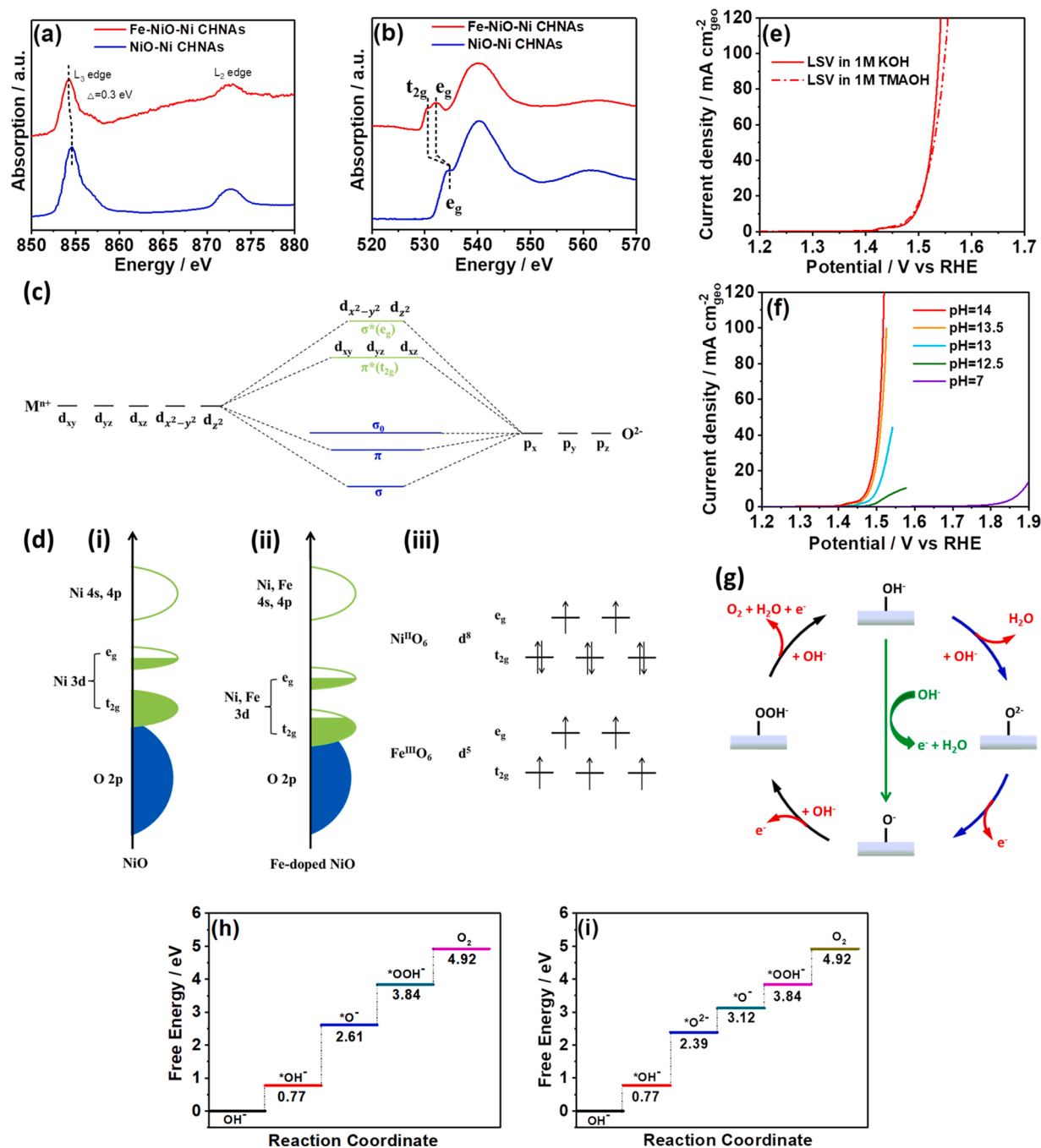


**Fig. 5.** (a) Ni L-edge and (b) O K-edge of Fe-NiO-Ni CHNAs and NiO-Ni CHNAs; (c) covalent mixing between M 3d and O 2p orbitals formed bonding, anti-bonding and non-bonding orbitals in the  $MO_6$  octahedron; (d) schematic diagram of the band structure of Fe-NiO-Ni CHNAs and NiO-Ni CHNAs; (e) LSV curves of Fe-NiO-Ni CHNAs in a 1 M KOH and TMAOH solution; (f) LSV curves of Fe-NiO-Ni CHNAs in a KOH solution with different pH range; (g) proton-electron transfer pathway and nonconcerted proton-electron transfer pathway of OER; Free energy diagrams of OER for Fe-doped-NiO with (h) proton-electron transfer pathway and (i) nonconcerted proton-electron transfer pathway.

exhibited a dominant metallic character, known as the M D-band (green parts in Fig. 5d (i and ii)). The band that originated from  $\sigma$ -bonding,  $\pi$ -bonding, and  $\sigma_0$ -nonbonding states exhibited a dominant  $O^{2-}$  character, called as O 2p band (blue parts in Fig. 5d (i and ii)). For NiO, the electronic configuration of  $Ni^{2+}$  was  $t_{2g}^6 e_g^2$  (Fig. 5d (iii)); thus, the d-band of  $t_{2g}$  was full and that of  $e_g$  was half full (Fig. 5d (i)). Therefore, the pre-edge in the O k-edge of NiO-Ni CHNAs should be assigned to the electron transition between O 1s and holes in the  $e_g$  band. For Fe-doped NiO, the electronic configuration of  $Fe^{3+}$  was  $t_{2g}^3 e_g^2$  (Fig. 5d (iii)). Fe-doping of NiO resulted in the D-band of  $t_{2g}$  not being full, and  $e_g$  remained half full (Fig. 5c (ii)). Therefore, the pre-edge in the O k-edge

of NiO-Ni CHNAs should be assigned to the electron transition from O 1s to the holes in both  $e_g$  and  $t_{2g}$  bands. For this reason, the pre-edge of the O k-edge split into double peaks in Fe-NiO-Ni CHNAs (Fig. 5b). Moreover, the negative shift of the pre-edge of the O k-edge in Fe-NiO-Ni CHNAs indicated that Fe-doping downshifted the M d-band (Fig. 5d (ii)). The downshift of the d-band center of M sites has been proven to lower the adsorption energy of intermediates and facilitate OER kinetics. [50] Moreover, negative shift of XPS in Ni 2p and Ni L-edge of Fe-NiO-Ni CHNAs indicates that the Ni charge is lower than its ionic charge (+2). The charge deviation of Ni suggests that the Ni-O bond in Fe-NiO-Ni CHNAs is not purely ionic but exhibits certain covalent character [8].

This phenomenon further implies that the downshift of M d-band also leads to Ni/Fe 3d and O 2p centers moving closer in Fe-NiO-Ni CHNAs, thus Fe-NiO-Ni CHNAs exhibits the greater M–O covalency [8]. (Fig. 5d (ii)). The enlarged M–O covalency promoted electron transfer between M cation and O adsorbates, facilitating the extraction of electrons from oxygen, thereby accelerating the OER process. [51]

### 3.3.3. OER pathway

The enlarged metal-oxygen covalency and the existence of O vacancies may trigger OER via the lattice oxygen oxidation mechanism (LOM) pathway, which involves negative  $O_2^-$  as intermediates rather than the conventional adsorbate evolution mechanism (AEM). [51] [52], Tetramethylammonium cation ( $TMA^+$ ) was employed as a chemical probe of  $O_2^-$  species for recognizing whether LOM occurred. [53] If the OER process occurred via LOM,  $TMA^+$  could attack the  $O_2^-$  species and strongly bind to the surface of the catalyst. In this way, the OER process could be inhibited, and the Raman characteristic peaks of  $TMA^+$  (458, 755 and  $952\text{ cm}^{-1}$ ) could be observed at the surface of the catalyst after the OER process being performed in 1 M TMAOH as an electrolyte. [52] However, the activities of Fe-NiO-Ni CHNAs and NiO-Ni CHNAs in 1 M TMAOH exhibited minimal change with no obvious inhibition compared with those in 1 M KOH (Fig. 5e and S40). Furthermore, the characteristic peaks of  $TMA^+$  could not be detected in either Fe-NiO-Ni CHNAs or NiO-Ni CHNAs after anodic scan in 1 M TMAOH (Figure S41). The above evidence clearly indicates that LOM was not triggered by enlarged metal-oxygen covalency and structural defects and that OER still occurred via conventional AEM.

Furthermore, the OER performance of Fe-NiO-Ni CHNAs and NiO-Ni CHNAs was examined in a KOH electrolyte with different pH range. The iR-corrected OER curves of Fe-NiO-Ni CHNAs and NiO-Ni CHNAs are shown in Figs. 5f and S42, respectively. It is apparent that catalytic activity exhibited strong pH dependence. The pH dependence indicated the existence of nonconcerted proton-electron transfer during the catalytic reaction. [51] According to the previous research, the nonconcerted proton-electron transfer pathway could be described as follows (Fig. 5g). First, the adsorbed  $OH^-$  on the oxide surface could be formed when basic oxides were immersed in an aqueous medium. [54] For so-called nonconcerted proton-electron transfer, the surface proton ( $M-OH^-$ , where M represents the active catalyst site) was firstly removed to form  $M-O^-$ . Subsequently, the electron is removed at the onset potential to form  $M-O^-$  (the blue arrow in Fig. 5g). This differs from the concerted proton-electron transfer pathway where  $M-O^-$  is directly formed as shown by the green arrow in Fig. 5g. Consequently, the reaction followed as the common steps of the surface  $M-O^-$  may be attacked by an  $OH^-$  to generate  $M-OOH^-$ . Eventually,  $M-OOH^-$  may be further attacked by  $OH^-$  to form  $O_2$  and  $M-OH^-$  (the black arrow in Fig. 5g). [55] The formation  $M-O^-$  via deprotonation of  $M-OH^-$  highly depends on the  $OH^-$  concentration in the electrolyte, low  $OH^-$  concentration impedes the deprotonation of  $M-OH^-$  thus retards the OER process. When pH of electrolyte is 7, the deprotonation almost cannot occur, which induces inactivation of OER. Thus the strong pH dependence of OER implies that the deprotonation step should be rate-determining step (RDS) in the mechanism. DFT calculation was employed to discuss the inevitability and rationality of the nonconcerted proton-electron transfer pathway during the catalytic reaction. As illustrated in Fig. 5h-i, the RDS of concerted proton-electron transfer pathway for Fe-doped-NiO is transformation of  $M-OH^-$  to  $M-O^-$  with energy barrier of 1.84 eV. However, the RDS is deprotonation of  $M-OH^-$  to form  $M-O^-$  with energy barrier of 1.62 eV for the nonconcerted proton-electron transfer pathway. Thus the nonconcerted proton-electron transfer pathway prefers to occur thermodynamically. Moreover, the free energy diagrams prove the deprotonation of  $M-OH^-$  is RDS, which perfectly verified above speculation expressing the strong pH dependence.

## 4. Conclusion

In summary, we engineered a novel multi-level structure of Fe-doped-NiO coupled Ni clusters hollow nanotubes arrays (Fe-NiO-Ni CHNAs) grown on CFC. The Fe-doped NiO phase was highly disordered and defect-rich, thereby creating abundant coordinative unsaturated active sites for OER. Moreover, Fe-doping downshifted the d-band of metal site, which is crucial for improving the OER catalytic activity. Furthermore, the unique 3D hollow nanotube arrays structure benefited the penetration and diffusion of active species and Ni clusters provided abundant heterostructures. These advantages endowed Fe-NiO-Ni CHNAs with excellent OER catalytic activity. The OER mechanism of Fe-NiO-Ni CHNAs obeyed the adsorbate evolution mechanism with a nonconcerted proton-electron transfer pathway, which was proven using TMAOH as a molecular probe and the catalytic activity exhibited a strong pH dependence. These results open up a new avenue for designing novel multi-nanostructures for application in electrocatalysis.

### Author contribution

Yaqi Lei and Tingting Xu: Performed the material characterization and OER testing; Shenghua Ye: Designed the experiments and performed theoretical analysis; Lirong Zheng: Performed XAFS tests and data analysis; Peng Liao, Wei Xiong Jing Hu, Yajie Wang and Jingpeng Wang: Help to complete the data processing; Xiangzhong Ren and Chuanxin He: Help to complete the academic writing; Qianling Zhang and Jianhong Liu: Convinced the experimental results and data discussion; Xueliang Sun: Supervised the writing, reviewing and editing.

### Declaration of Competing Interest

The authors declare that they have no known competing financial interests or personal relationships that could have appeared to influence the work reported in this paper.

### Acknowledgements

Ya-qi Lei, Ting-ting Xu and Sheng-hua Ye contributed equally to this work. We appreciate the financial support of Shenzhen Basic Research Project (No. JCYJ20170818092720054, JCYJ20190808145203535, JCYJ20190808144413257), National Natural Science Foundation of China (No. 21671136), Postdoctoral Science Foundation of China (No. 2019M663085), Shenzhen Technology Development Program (No. JSGG20160328151657828, XCL201110060), the Major Industrial Projects of Shenzhen (s2017001850011), and the Project of Natural Science Foundation of Guangdong Province (No. 2020A1515010380).

### Appendix A. Supplementary data

Supplementary material related to this article can be found, in the online version, at doi:<https://doi.org/10.1016/j.apcatb.2020.119809>.

## References

- [1] T. Hisatomi, J. Kubota, K. Domen, Recent advances in semiconductors for photocatalytic and photoelectrochemical water splitting, *Chem. Soc. Rev.* 43 (2014) 7520–7535.
- [2] F. Song, L. Bai, A. Moysiadou, S. Lee, C. Hu, L. Liardet, X. Hu, Transition metal oxides as electrocatalysts for the oxygen evolution reaction in alkaline solutions: an application-inspired renaissance, *J. Am. Chem. Soc.* 140 (2018) 7748–7759.
- [3] B.M. Hunter, H.B. Gray, A.M. Muller, Earth-abundant heterogeneous water oxidation catalysts, *Chem. Rev.* 116 (2016) 14120–14136.
- [4] D. Chen, J.W. Zhu, X.Q. Mu, R.L. Cheng, W.Q. Li, S.L. Liu, Z.H. Pu, C. Lin, S.C. Mu, Nitrogen-Doped carbon coupled  $FeNi_3$  intermetallic compound as advanced bifunctional electrocatalyst for OER, ORR and zn-air batteries, *Appl. Catal. B Environ.* 268 (2020), 118729.
- [5] M.W. Kanan, D.G. Nocera, In situ formation of an oxygen-evolving catalyst in neutral water containing phosphate and  $Co^{2+}$ , *Science* 321 (2008) 1072.

- [6] Q. Shi, C. Zhu, D. Du, Y. Lin, Robust noble metal-based electrocatalysts for oxygen evolution reaction, *Chem. Soc. Rev.* 48 (2019) 3181–3192.
- [7] N.-T. Suen, S.-F. Hung, Q. Quan, N. Zhang, Y.-J. Xu, H.M. Chen, Electrocatalysis for the oxygen evolution reaction: recent development and future perspectives, *Chem. Soc. Rev.* 46 (2017) 337–365.
- [8] S. Sun, Y. Sun, Y. Zhou, S. Xi, X. Ren, B. Huang, H. Liao, L.P. Wang, Y. Du, Z.J. Xu, Shifting oxygen charge towards octahedral metal: a way to promote water oxidation on cobalt spinel oxides, *Angew. Chem. Int. Ed.* 58 (2019) 6042–6047.
- [9] A. Bergmann, E. Martinez-Moreno, D. Teschner, P. Cherev, M. Gliech, J.F. de Araújo, T. Reier, H. Dau, P. Strasser, Reversible amorphization and the catalytically active state of crystalline  $\text{Co}_3\text{O}_4$  during oxygen evolution, *Nat. Commun.* 6 (2015) 8625.
- [10] C. Guan, X. Liu, W. Ren, X. Li, C. Cheng, J. Wang, Rational design of metal-organic framework derived hollow  $\text{NiCo}_2\text{O}_4$  arrays for flexible supercapacitor and electrocatalysis, *Adv. Energy Mater.* 7 (2017), 1602391.
- [11] S. Lei, Q.H. Li, Y. Kang, Z.G. Gu, J. Zhang, Epitaxial growth of oriented prussian blue analogue derived well-aligned  $\text{CoFe}_2\text{O}_4$  thin film for efficient oxygen evolution reaction, *Appl. Catal. B: Environ.* 245 (2019) 1–9.
- [12] A. Indra, P.W. Menezes, N.R. Sahaie, A. Bergmann, C. Das, M. Tallarida, D. Schmeißer, P. Strasser, M. Driess, Unification of catalytic water oxidation and oxygen reduction reactions: amorphous beat crystalline cobalt Iron oxides, *J. Am. Chem. Soc.* 136 (2014) 17530–17536.
- [13] C. Wei, R.R. Rao, J. Peng, B. Huang, L.E.L. Stephens, M. Risch, Z.J. Xu, Y. Shao-Horn, Recommended practices and benchmark activity for hydrogen and oxygen electrocatalysis in water splitting and fuel cells, *Adv. Mater.* 31 (2019), 1806296.
- [14] S. Sun, H. Li, Z.J. Xu, Impact of surface area in evaluation of catalyst activity, *Joule* 2 (2018) 1024–1027.
- [15] Y. Liu, H. Wang, D. Lin, C. Liu, P.-C. Hsu, W. Liu, W. Chen, Y. Cui, Electrochemical tuning of olivine-type lithium transition-metal phosphates as efficient water oxidation catalysts, *Energy Environ. Sci.* 8 (2015) 1719–1724.
- [16] Z.S. Li, L. Lv, X. Ao, J.-G. Li, H.C. Sun, P.D. An, X.Y. Xue, Y. Li, M. Liu, C.D. Wang, M.L. Liu, An effective method for enhancing oxygen evolution kinetics of  $\text{LaMO}_3$  ( $M = \text{Ni}, \text{Co}, \text{Mn}$ ) perovskite catalysts and its application to a rechargeable zinc–air battery, *Appl. Catal. B: Environ.* 262 (2020) 118291.
- [17] L.Q. Gui, Z.B. Wang, K. Zhang, B.B. He, Y.Z. Liu, W. Zhou, J.M. Xu, Q. Wang, L. Zhao, Oxygen vacancies-rich  $\text{Ce}_{0.9}\text{Gd}_{0.1}\text{O}_{2-\delta}$  decorated  $\text{Pr}_{0.5}\text{Ba}_{0.5}\text{CoO}_{3-\delta}$  bifunctional catalyst for efficient and long-lasting rechargeable Zn–air batteries, *Appl. Catal. B: Environ.* 266 (2020), 118656.
- [18] G. Li, S.E. Hou, L.Q. Gui, F.L. Feng, D.B. Zhang, B.B. He, L. Zhao, Carbon quantum dots decorated  $\text{Ba}_{0.5}\text{Sr}_{0.5}\text{Co}_{0.8}\text{Fe}_{0.2}\text{O}_{3-\delta}$  perovskite nanofibers for boosting oxygen evolution reaction, *Appl. Catal. B: Environ.* 257 (2019), 117919.
- [19] Y. Zhou, S. Sun, C. Wei, Y. Sun, P. Xi, Z. Feng, Z.J. Xu, Significance of engineering the octahedral units to promote the oxygen evolution reaction of spinel oxides, *Adv. Mater.* 31 (2019), 1902509.
- [20] T. Wu, S. Sun, J. Song, S. Xi, Y. Du, B. Chen, W.A. Sasangka, H. Liao, C.L. Gan, G. G. Scherer, L. Zeng, H. Wang, H. Li, A. Grimaud, Z.J. Xu, Iron-facilitated dynamic active-site generation on spinel  $\text{CoAl}_2\text{O}_4$  with self-termination of surface reconstruction for water oxidation, *Nat. Catal.* 2 (2019) 763–772.
- [21] C. Feng, M.B. Faheem, J. Fu, Y.Q. Xiao, C.L. Li, Y.B. Li, Fe-based electrocatalysts for oxygen evolution reaction: progress and perspectives, *ACS Catal.* 10 (2020) 4019–4047.
- [22] J.W. Wan, W.X. Chen, C. Chen, Q. Peng, D.S. Wang, Y.D. Li, Facile synthesis of  $\text{CoNi}_x$  nanoparticles embedded in nitrogen–carbon frameworks for highly efficient electrocatalytic oxygen evolution, *Chem. Commun.* 53 (2017) 12177–12180.
- [23] H. Zhang, H.Y. Li, B. Akram, X. Wang, Fabrication of NiFe layered double hydroxide with well-defined laminar superstructure as highly efficient oxygen evolution electrocatalysts, *Nano Res.* 12 (2019) 1327–1331.
- [24] M.B. Stevens, L.J. Enman, E.H. Korkus, J. Zaffran, C.D.M. Trang, J. Asbury, M. G. Kast, M.C. Toroker, S.W. Boettcher, Ternary Ni-Co-Fe oxyhydroxide oxygen evolution catalysts: intrinsic activity trends, electrical conductivity, and electronic band structure, *Nano Res.* 12 (2019) 2288–2295.
- [25] S. Yagi, I. Yamada, H. Tsukasaki, A. Seno, M. Murakami, H. Fujii, H. Chen, N. Umezawa, H. Abe, N. Nishiyama, S. Mori, Covalency-reinforced oxygen evolution reaction catalyst, *Nat. Commun.* 6 (2015) 8249.
- [26] N. Li, D.K. Bediako, R.G. Hadt, D. Hayes, T.J. Kempa, F. von Cube, D.C. Bell, L. X. Chen, D.G. Nocera, Influence of iron doping on tetravalent nickel content in catalytic oxygen evolving films, *Proc. Natl Acad. Sci. USA* 114 (2017) 1486–1491.
- [27] M. Görlin, P. Cherev, J. Ferreira de Araújo, T. Reier, S. Dresch, B. Paul, R. Krähnert, H. Dau, P. Strasser, Oxygen evolution reaction dynamics, faradaic charge efficiency, and the active metal redox states of Ni–Fe oxide water splitting electrocatalysts, *J. Am. Chem. Soc.* 138 (2016) 5603–5614.
- [28] M. Tadic, D. Nikolic, M. Panjan, G.R. Blake, Magnetic properties of NiO (nickel oxide) nanoparticles: blocking temperature and Neel temperature, *J. Alloys. Compd.* 647 (2015) 1061–1068.
- [29] H.J. Lee, S. Back, J.H. Lee, S.H. Choi, Y. Jung, J.W. Choi, Mixed transition metal oxide with vacancy-induced lattice distortion for enhanced catalytic activity of oxygen evolution reaction, *ACS Catal.* 9 (2019) 7099–7108.
- [30] G. Kresse, J. Furthmüller, Efficient iterative schemes for ab initio total-energy calculations using a plane-wave basis set, *Phys. Rev. B* 54 (1996) 11169–11186.
- [31] G. Kresse, J. Hafner, Ab initio molecular dynamics for liquid metals, *Phys. Rev. B Condens. Matter* 47 (1993) 558–561.
- [32] J.P. Perdew, M. Ernzerhof, K. Burke, Rationale for mixing exact exchange with density functional approximations, *J. Chem. Phys.* 105 (1996) 9982–9985.
- [33] J.P. Perdew, K. Burke, M. Ernzerhof, Generalized gradient approximation made simple, *Phys. Rev. Lett.* 77 (1996) 3865–3868.
- [34] S. Grimme, Semiempirical GGA-type density functional constructed with a long-range dispersion correction, *J. Comput. Chem.* 27 (2006) 1787–1799.
- [35] F. Guo, Y. Wu, H. Chen, Y. Liu, L. Yang, X. Ai, X. Zou, High-performance oxygen evolution electrocatalysis by boronized metal sheets with self-functionalized surfaces, *Energy Environ. Sci.* 12 (2019) 684–692.
- [36] G. Zhou, D.-W. Wang, L.-C. Yin, N. Li, F. Li, H.-M. Cheng, Oxygen bridges between NiO nanosheets and graphene for improvement of Lithium storage, *ACS Nano* 6 (2012) 3214–3223.
- [37] W.J. Duan, S.H. Lu, Z.L. Wu, Y.S. Wang, Size effects on properties of NiO nanoparticles grown in Alkaline salts, *J. Phys. Chem. C* 116 (2012) 26043–26051.
- [38] M.W. Louie, A.T. Bell, An investigation of thin-film Ni–Fe oxide catalysts for the electrochemical evolution of oxygen, *J. Am. Chem. Soc.* 135 (2013) 12329–12337.
- [39] D.L.A. deFaria, S.V. Silva, M.T. deOliveira, Raman microspectroscopy of some iron oxides and oxyhydroxides, *J. Raman Spectrosc.* 28 (1997) 873–878.
- [40] F. Lei, Y. Sun, K. Liu, S. Gao, L. Liang, B. Pan, Y. Xie, Oxygen vacancies confined in ultrathin indium oxide porous sheets for promoted visible-light water splitting, *J. Am. Chem. Soc.* 136 (2014) 6826–6829.
- [41] J. Bao, X. Zhang, B. Fan, J. Zhang, M. Zhou, W. Yang, X. Hu, H. Wang, B. Pan, Y. Xie, Ultrathin spinel-structured nanosheets rich in oxygen deficiencies for enhanced electrocatalytic water oxidation, *Angew. Chem. Int. Ed.* 54 (2015) 7399–7404.
- [42] Y.P. Liu, Q.J. Li, R. Si, G.D. Li, W. Li, D.P. Liu, D.J. Wang, L. Sun, Y. Zhang, X. X. Zou, Coupling sub-nanometric copper clusters with quasi-amorphous cobalt sulfide yields efficient and robust electrocatalysts for water splitting reaction, *Adv. Mater.* 29 (2017), 1606200.
- [43] J. Bak, H. Bin Bae, S.-Y. Chung, Atomic-scale perturbation of oxygen octahedra via surface ion exchange in perovskite nickelates boosts water oxidation, *Nat. Commun.* 10 (2019) 2713.
- [44] M. Lee, H. Oh, M. –K. Cho, J. Ahn, Y.J. Hwang, B.K. Min, Activation of a Ni electrocatalyst through spontaneous transformation of nickel sulfide to nickel hydroxide in an oxygen evolution reaction, *Appl. Catal. B: Environ.* 233 (2018) 130–135.
- [45] B. Wang, C. Tang, H.-F. Wang, X. Chen, R. Cao, Q. Zhang, A nanosized CoNi Hydroxide@Hydroxysulfide core–Shell heterostructure for enhanced oxygen evolution, *Adv. Mater.* 31 (2019), 1805658.
- [46] C. Hu, L. Zhang, Z.-J. Zhao, A. Li, X. Chang, J. Gong, Synergism of geometric construction and electronic regulation: 3D Se–(NiCo) $\text{S}_x$ /(OH) $_x$  nanosheets for highly efficient overall water splitting, *Adv. Mater.* 30 (2018), 1705538.
- [47] D. Wu, Y. Wei, X. Ren, X. Ji, Y. Liu, X. Guo, Z. Liu, A.M. Asiri, Q. Wei, X. Sun, Co(OH) $_2$  nanoparticle-encapsulating conductive nanowires array: room-temperature electrochemical preparation for high-performance water oxidation electrocatalysis, *Adv. Mater.* 30 (2018), 1705366.
- [48] S.H. Ye, Y. Zhang, W. Xiong, T.T. Xu, P. Liao, P.Y. Zhang, X.Z. Ren, C.X. He, L. R. Zheng, X.P. Ouyang, Q.L. Zhang, J.H. Liu, Construction of tetrahedral  $\text{CoO}_4$  vacancies for activating the high oxygen evolution activity of  $\text{Co}_{3-x}\text{O}_{4-\delta}$  porous nanosheet arrays, *Nanoscale* 12 (2020) 11079–11087.
- [49] C.H.M. van Oversteeg, H.Q. Doan, F.M.F. de Groot, T. Cuk, In situ X-ray absorption spectroscopy of transition metal based water oxidation catalysts, *Chem. Soc. Rev.* 46 (2017) 102–125.
- [50] Z. Xue, X. Li, Q. Liu, M. Cai, K. Liu, M. Liu, Z. Ke, X. Liu, G. Li, Interfacial electronic structure modulation of NiTe nanoarrays with NiS nanodots facilitates electrocatalytic oxygen evolution, *Adv. Mater.* 31 (2019), 1900430.
- [51] Y. Duan, S. Sun, Y. Sun, S. Xi, X. Chi, Q. Zhang, X. Ren, J. Wang, S.J.H. Ong, Y. Du, L. Gu, A. Grimaud, Z.J. Xu, Mastering surface reconstruction of metastable spinel oxides for better water oxidation, *Adv. Mater.* 31 (2019), 1807898.
- [52] A. Grimaud, O. Diaz-Morales, B. Han, W.T. Hong, Y.-L. Lee, L. Giordano, K. A. Stoerzinger, M.T.M. Koper, Y. Shao-Horn, Activating lattice oxygen redox reactions in metal oxides to catalyze oxygen evolution, *Nat. Chem.* 9 (2017) 457–465.
- [53] Z.-F. Huang, J. Song, Y. Du, S. Xi, S. Dou, J.M.V. Nsanzimana, C. Wang, Z.J. Xu, X. Wang, Chemical and structural origin of lattice oxygen oxidation in Co–Zn oxyhydroxide oxygen evolution electrocatalysts, *Nat. Energy* 4 (2019) 329–338.
- [54] J.B. Goodenough, R. Manoharan, M. Paranthaman, Surface protonation and electrochemical activity of oxides in aqueous solution, *J. Am. Chem. Soc.* 112 (1990) 2076–2082.
- [55] X. Li, H. Wang, Z. Cui, Y. Li, S. Xin, J. Zhou, Y. Long, C. Jin, J.B. Goodenough, Exceptional oxygen evolution reactivities on  $\text{CaCoO}_3$  and  $\text{SrCoO}_3$ , *Sci. Adv.* 5 (2019) eaav6262.